HCIT Broadband Contrast Performance Sensitivity Studies

Erkin Sidick*, Stuart Shaklan, Kunjithapatham Balasubramanian
Jet Propulsion Laboratory, California Institute of Technology, 4800 Oak Grove Drive, Pasadena, CA 91109, USA

ABSTRACT

The High Contrast Imaging Testbed (HCIT) at the Jet Propulsion Laboratory employs a broadband wavefront correction algorithm called Electric Field Conjugation (EFC) to obtain the required 10^{-10} contrast. This algorithm works with one deformable mirror (DM) to estimate the electric-field to be controlled, and with one or multiple DM's to create a "dark-hole" in a predefined region of the image plane where terrestrial planets would be found. We have investigated the effects of absorbing dust particles on a flat optic, absorbing spots on the occulting mask, dead actuators on the DM, and the effects of control bandwidth on the efficiency of the EFC algorithm in a Lyot coronagraph configuration. The structural design of the optical system as well as the parameters of various optical elements used in the analysis is drawn from those of the HCIT system that have been implemented with one DM. The simulation takes into account the surface errors of various optical elements. Results of some of these studies have been verified by actual measurements.

Key words: Coronagraphy, adaptive optics, space telescopes, exoplanets

1. INTRODUCTION

The High-contrast imaging testbed (HCIT) at JPL is the Exoplanet Exploration Program's primary platform for experimentation [1-3]. It is used to provide laboratory validation of key technologies as well as demonstration of a flight-traceable approach to implementation. It employs a broadband wavefront correction algorithm called Electric Field Conjugation (EFC) to obtain the required 10^{-10} contrast [4]. This algorithm works with one or multiple deformable mirrors (DM's) to create a "dark-hole" in a predefined region of the image plane where terrestrial planets would be found. It achieves the desired high contrast level in two stages. The first is the estimation stage. In this stage, the algorithm provides an estimate of the aberrated complex electric field (e-field) in the image plane based on pairs of images taken at the final image plane using different DM surface configurations. The second is the correction or EFC stage. In this stage the algorithm generates a correction based on the e-field estimated in the first stage. The correction is then applied to the DM actuators to null the image e-field in the predefined dark-hole region.

We have investigated the effects of absorbing particles/spots, dead actuators and control bandwidth on the system performance and the efficiency of the EFC algorithm in a Lyot coronagraph configuration. Considered cases include absorbing particles on the surface of a flat optic, i.e., a fold-mirror, absorbing spots on the surface of the occulting mask, dead actuators on the DM, and varying control bandwidths. The structural design of the optical system as well as the parameters of various optical elements used in the analysis is drawn from those of the HCIT system that have been implemented with one DM. The simulation takes into account the surface errors of various optics. The optical simulation algorithm uses MACOS (Modeling and Analysis for Controlled Optical Systems) as its analytic tool [5]. Hence it is capable of performing full three-dimensional near-field diffraction analysis on HCIT's optical model. Results of some of these studies have been verified by actual measurements. Other types of errors were investigated and reported earlier [6].

2. BACKGROUND

2.1 The HCIT Optical System

The schematic diagram of the HCIT layout in the *xz*-plane is shown in Figure 1. Artificial starlight is created by a 5μm pinhole illuminated by an optical fiber. We assume a broadband light source centered at wavelength λ=800nm and having a bandwidth of ±5%, or $\Delta\lambda$=80nm. An off-axis parabolic mirror (OAP1) collimates the light from the pinhole

*Erkin.Sidick@jpl.nasa.gov; Phone 1 818 393-7585; Fax 1 818 393-9471; www.jpl.nasa.gov

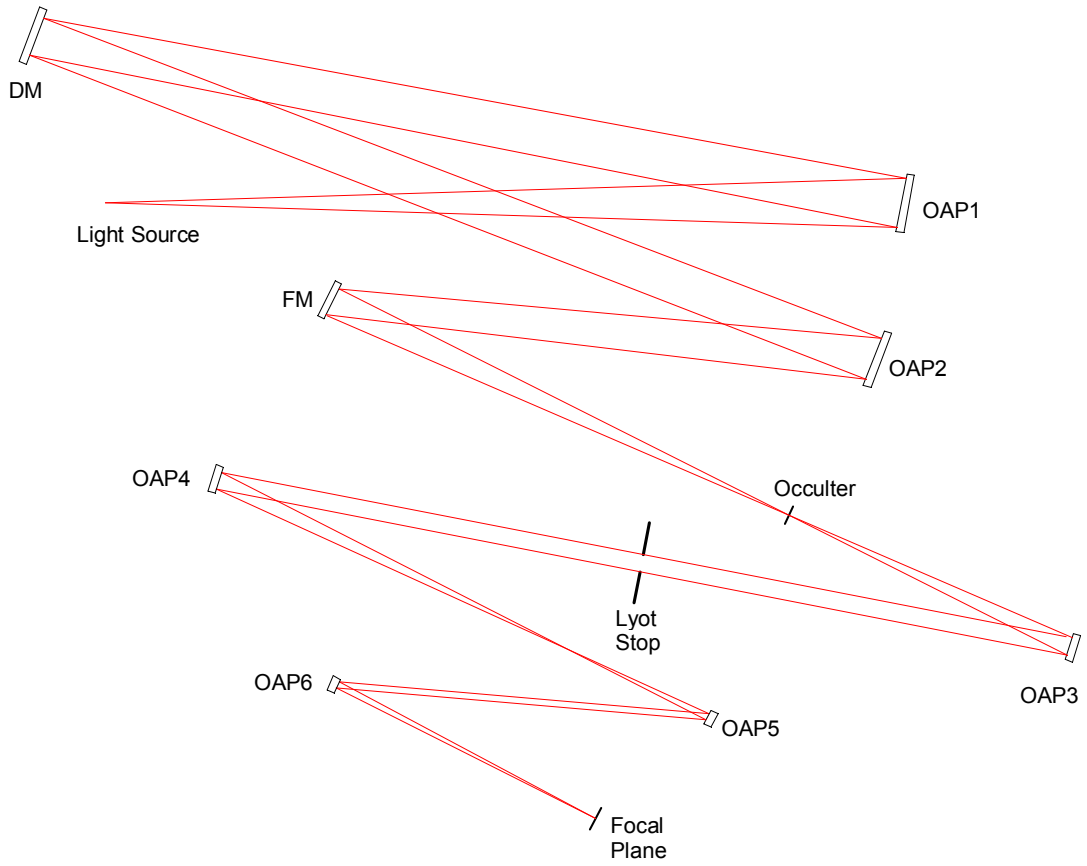

Figure 1. Schematic diagram of the High Contrast Imaging Testbed (HCIT) layout. The light source ("starlight") is a 5μm pinhole illuminated by an optical fiber, and a CCD science camera is located at the back focal plane for detecting the image of the "starlight".

and directs it to a high-density, 64x64 actuator deformable mirror (DM), which performs wavefront control. A circular aperture mask on the DM defines the system pupil of the HCIT, and can have a diameter of up to D=64mm. However, the current HCIT was implemented with D=48mm inscribed in an area covered by 48x48 actuators, so we will use this D value in the simulations of this paper. After the DM, the collimated light is imaged onto the focal plane of the occulting mask by OAP2 and a flat-mirror (FM). The occulting mask attenuates the starlight, and almost has no effect on the light of a planet if present. The "back-end" of the system, from the occulting mask to the back focal plane, supports experimentation with diverse coronagraph configurations and apodizations. OAP3 re-collimates the light passing through the occulter mask and forms a same-size sharp image of the DM pupil at the Lyot plane. A Lyot stop blocks the ring-like residual light diffracted off the occulting mask while letting most of the planet light through. After OAP4 forms an image from the remaining stellar and planet lights, it is then magnified (M ≈3) by the OAP5-OAP6 pair for proper sampling on the CCD science camera located at the back focal plane. More information on the HCIT and the DM can be found in Refs. [1-3].

2.2 Occulting Mask

The HCIT uses a modified one-dimensional band-limited occulter whose OD profile at wavelength λ = 800nm is truncated and smoothed by convolution with a Gaussian function. This smoothed pattern is described in detail in Refs. [7-8]. Specifically, the sinc^2 intensity transmission profile is $T_{\text{sinc}}(x) = \{1-[\sin(\pi x/w)/(\pi x/w)]^2\}^2$, $\text{OD}_{\text{sinc}}(x) = -\log_{10} T_{\text{sinc}}(x)$, with w = 142μm. The truncation and smoothing gives $\text{OD}_{\text{rel}}(x) = \min[\text{OD}_{\text{sinc}}(x), 8] \otimes G(x)$ with $G(x) = (2\pi\sigma^2)^{-1/2} \exp[-x^2/(2\sigma^2)]$, σ = 9μm. For practical reasons, the maximum transmission is often less than unity, so the final transmission is $T(x) = T_0\ 10^{-\text{ODrel}(x)}$, for some maximum transmission T_0. The above two OD profiles are shown graphically in Fig. 2(a). The spatially-varying transmission profile is optically realized by spatially varying the thicknesses of Ni layers, deposited on a fused quartz substrate. Because Ni has a large index of refraction (n ~ 2.5 at

800nm), regions of the occulter with higher OD (lower transmission, thicker Ni) also have a greater optical path length in transmission than low OD regions. The spatially-varying transmitted e-field is therefore complex-valued. In addition to the spatial variations in OD and phase, the OD and phase also vary with wavelength. Ni was chosen for this application because its OD and phase vary less with wavelength than other practical materials, as described in Ref. [9]. We will include the dispersion of both occulter OD and phase in our simulations. The profile of the occulter phase at λ=800nm, ϕ(800) is also shown in Fig. 2(a) in radians. Figure 2(b) shows the variation of the occulter OD at five wavelength values relative to that at λ=800nm, or the OD dispersion. The occulter phase dispersion is weaker than the OD dispersion, and the ϕ(λ) - ϕ(800) has the largest value of -0.012 radians at the center of occulter and at λ = 768nm. For this occulter, $T(x) = 0.5$ at $x/f = 3.3\lambda/D$, where $D = 48$mm is the diameter of the system clear aperture and f is the focal length. The front end F-number (F/#) of this optical system is 31.25.

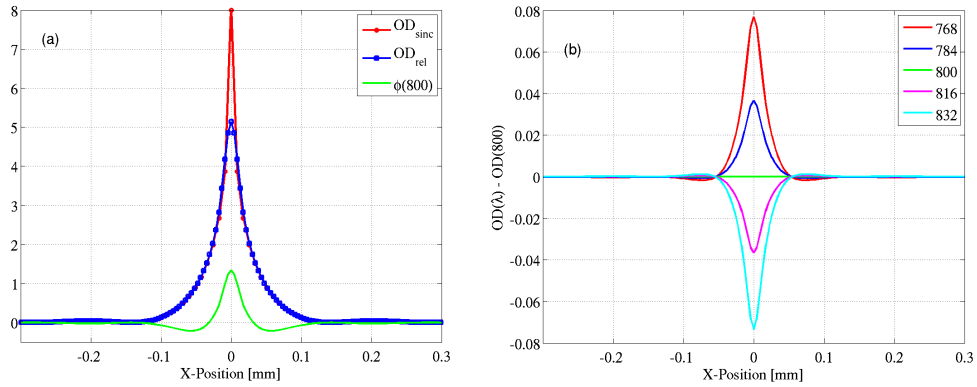

Figure 2. (a) The x-profiles of occulter Optical Densities, OD_{sinc} and OD_{rel}, as well as transmitted occulter phase at λ = 800nm, ϕ(800), where the latter is given in radians. (b) Occulter OD dispersion, where the figure legend shows five wavelength values in nm. These parameters correspond to a linear-sinc^2 occulting mask consisting of Ni deposited on a fused quartz substrate. .

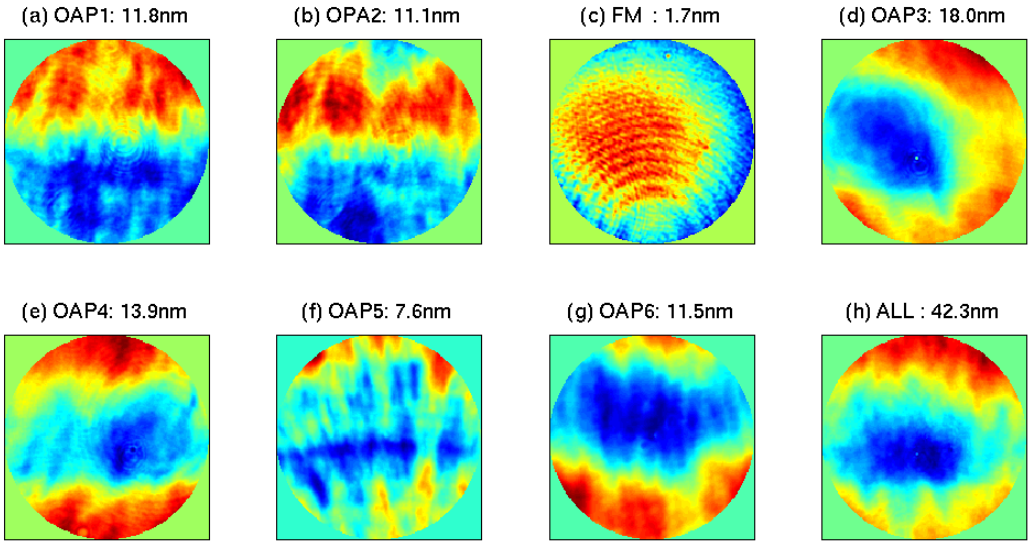

Figure 3. Surface height errors of various optics exhibited as OPD (Optical Path Difference) at the exit-pupil. The part (h) is the OPD when the surface height errors of all seven optics are included. The number included in each figure's title is the RMS (root-mean-square) value of the corresponding OPD map.

2.3 Other Optical Components

The DM used on the HCIT has 64x64 actuators arrayed on a 1mm pitch. Its description is similar to the 32x32 actuator DM described in detail in Ref. [1], and will not be repeated here.

Our Lyot stop is made from a simple blackened piece of sheet metal with a sharp edge. Its opening (Lyot stop aperture) has an eye-shape defined by two circles that are shifted with respect to each other in the horizontal direction by a distance of ε in units of D. The value of ε needs to be chosen based on the value of the occulting mask width parameter w, and ε=0.36 in this paper.

In our simulations, we include the surface errors of the six OAP's and the FM shown in Figs. 3(a-g). These are OPD (Optical Path-Difference) maps obtained at the system exit pupil by "turning-on" one surface height error map at a time. The part (h) is the total OPD at the exit-pupil obtained when the surface height errors of all seven optics are included in the simulation. Some optics on the current HCIT have surface height errors different from the above, and we used them here just to introduce some realistic surface errors into the HCIT optical model.

2.4 Definitions of Half Dark-Hole Area and Contrast

For the current optical system with only one DM, we carry out wavefront control (WFC) over a region Ω_c, where Ω_c is a rectangular half dark-hole region bound by $[X_1\ X_2\ Y_1\ Y_2] = [3.5\ 12\ -12\ 12]\lambda/D$, $X = x/f$, $Y = y/f$, and x and y are the horizontal and the vertical position variables on the corresponding image-plane. We will evaluate the performance of the HCIT using either the normalized intensity,

$$I_n(x,y) = I(x,y)/I_0, \tag{1}$$

or the contrast,

$$C(x,y) = I_n(x,y)[T_0/T(x,y)] = [I(x,y)/I_0][T_0/T(x,y)], \tag{2}$$

where $I(x,y)$ is the image intensity of the occulted star, and I_0 is the maximum value of the un-occulted star intensity, $T(x,y)$ is the occulter transmittance, and T_0 is the maximum value of the $T(x,y)$. We will keep track of the following three contrast quantities in this paper: (i) C_b, the mean contrast inside a "Big" rectangular region Ω_b defined by $[X_1\ X_2\ Y_1\ Y_2] = [4\ 11\ -11\ 11]\lambda/D$. (ii) C_s, the mean contrast inside a "Small" square region Ω_s defined by $[X_1\ X_2\ Y_1\ Y_2] = [4\ 5\ -0.5\ 0.5]\lambda/D$. (iii) C_m, the "Maximum" contrast value inside the small square region Ω_s. Similarly, we also use I_b, I_s and I_m to denote the big-region mean, the small-region mean, and the small-region maximum of the normalized intensity $I_n(x,y)$. The nominal Intensity values obtained for a narrowband light with $\lambda_0 = 800\text{nm}$ and the error-free optical system (even the occulter phase is set to zero) without conducting any wavefront control are $[I_b\ I_s\ I_m] = [0.37\ 2.8\ 3.8]\times 1\text{E}-8$, respectively. When the phase errors of the seven optics as well as the occulter phase are included in simulation, the above intensity values change to $[0.39\ 4.7\ 9.3]\times 1\text{E}-5$, respectively. If we use the designed transmission profile $T_{\text{sinc}}(x)$ of the occulter, we obtain much better contrast values: $[0.77\ 8.7\ 11.9]\times 1\text{E}-12$. This is similar to what we reported in Ref. [6]. This is because $\text{OD}_{\text{max}} = 8$ for $T_{\text{sinc}}(x)$ at the center of the occulter, while $T(x)$ has only $\text{OD}_{\text{max}} = 5.14$.

2.5 About the Wavefront Control (WFC) Algorithm

In this paper, we use a control algorithm similar to the "minimum-wavefront and optimal control compensator" described in detail in Ref. [10]. This approach is also called "Actuator regularization" [4]. The WFC algorithm described in Ref. [10] uses the wavefront at the system exit pupil as its input, and calculates the actuator commands as its output. In the present case we set the DM actuators to superpose the negative of the e-field onto the image plane, with a goal to make the image intensity zero on the region Ω_c. Therefore, the WFC algorithm uses an e-field column-vector $\vec{\mathbf{e}}$ as its input, where

$$\vec{\mathbf{e}} = \begin{bmatrix} \Re(\vec{\mathbf{E}}) \\ \Im(\vec{\mathbf{E}}) \end{bmatrix}. \tag{3}$$

The joint cost function now becomes as

$$J = \frac{1}{2}\left(\vec{\mathbf{e}}^T\vec{\mathbf{e}} + \gamma_{\mathrm{wu}}\vec{\mathbf{u}}^T\vec{\mathbf{u}}\right), \tag{4}$$

and the gain matrix $\widetilde{\mathbf{G}}$ is obtained from

$$\widetilde{\mathbf{G}} = \left[\widetilde{\mathbf{S}}^T\widetilde{\mathbf{S}} + \gamma_{\mathrm{wu}}\widetilde{\mathbf{I}}\right]^{-1}\widetilde{\mathbf{S}}^T. \tag{5}$$

In Eq. (3), $\vec{\mathbf{E}}$ is the column-vector of the complex e-field on region Ω_c. It is formed by stacking the elements of the complex e-field on region Ω_c in a certain order, as was explained in Eq. (1) of Ref. [10]. The $\Re(\vec{\mathbf{E}})$ and the $\Im(\vec{\mathbf{E}})$ are the real and the imaginary parts of $\vec{\mathbf{E}}$, respectively. In Eq. (5), the $\widetilde{\mathbf{S}}$ is the sensitivity matrix consisting of the influence functions of all actuators. The MACOS simulation tool calculates the complex e-field at the final focal plane directly. Therefore, the e-field estimation step is actually not needed in our simulation and we will not use it in this paper. The simulation creates a 512x512-pixel image map, with ~4 pixels per $f\lambda/D$. Considering only the pixels in the dark hole gives an e-field vector, $\vec{\mathbf{e}}$, having a size of 3521x1 pixels per wavelength on the average. There are a total of 2304 DM actuators in the current 1-DM system, but we use only 1907 (~83%) actuators excluding those with zero or very weak influences.

3. SIMULATION RESULTS

We now describe our simulation results. We start with the nominal case where only the optical surface errors and the occulter phase are included in the simulation.

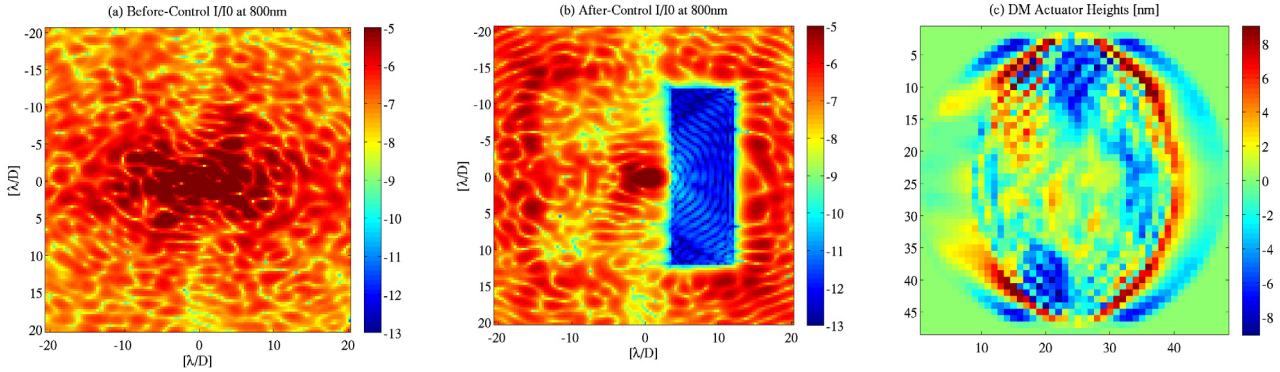

Figure 3. Log-scale PSF (a) before WFC and (b) after 30-iterations WFC at λ_3 = 800nm, where the units of the horizontal- and the vertical-axes are λ/D. (c) Actuator-height map obtained at the end of broadband WFC, where the units of the horizontal- and the vertical-axes are mm.

3.1 Nominal Case

We use the EFC-based broadband wavefront correction algorithm described in Ref. [4] in our simulations. The broadband sensitivity-matrix $\widetilde{\mathbf{S}}$ consists of three monochromatic sensitivity matrices corresponding to wavelengths λ=768, 800nm and 832nm, respectively. That is, we carry out the WFC at the above three wavelengths simultaneously, by obtaining one set of DM solutions from the e-fields corresponding to the three wavelengths. These wavelengths correspond to the center wavelengths of three of the five 2% bandpass filters [8] employed on the HCIT and centered at λ = 768, 784, 800, 816 and 832nm, respectively. To obtain a 8%-broadband $I_n(x,y)$ map, we calculate the final image plane intensity maps at the above five wavelengths separately first, then average them to obtain the broadband image intensity map. To calculate the 10%-broadband contrast, we add two new wavelengths to the above list, λ=760 and 840nm, and average the resulting seven intensity maps.

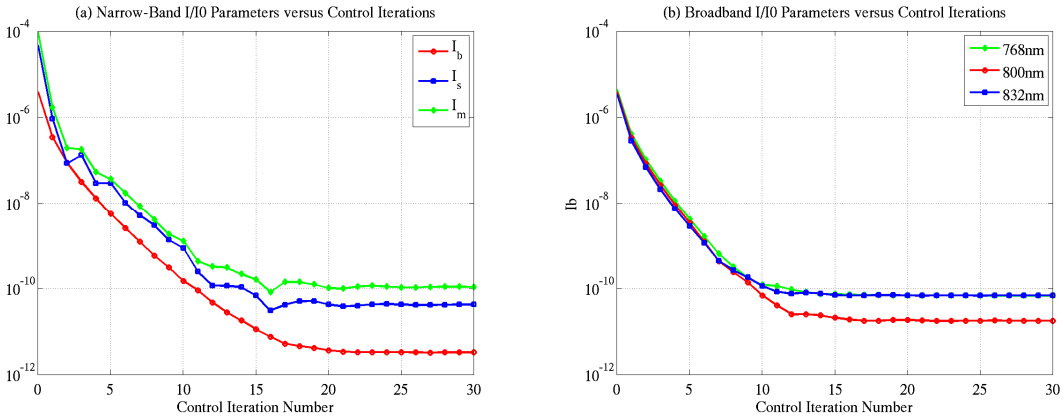

Figure 4. I_b, I_s and I_m versus control iteration number. (a) Monochromatic I_b, I_s and I_m at λ_3=800nm. (b) I_b at three different wavelengths obtained with a single set of DM solutions.

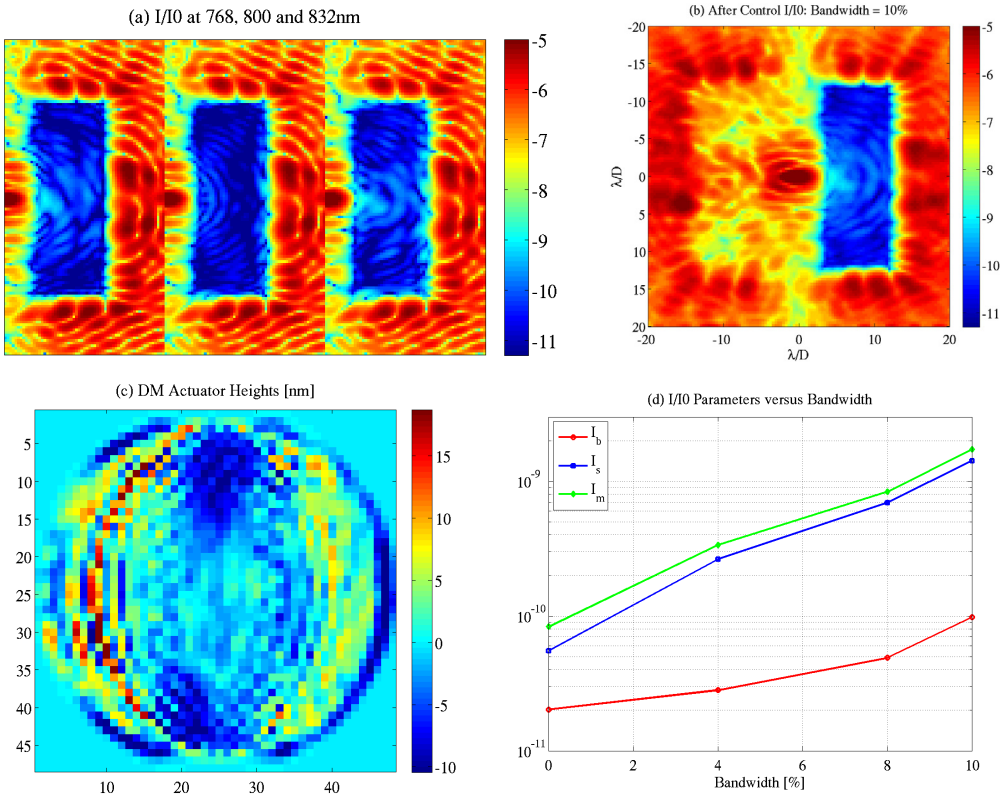

Figure 5. (a) Log-scale $I_n(x,y)$ maps obtained after 30-iterations of broadband-WFC at three wavelengths. (b) Log-scale 10%-broadband $I_n(x,y)$ map corresponding to part (a). (c) DM heights leading to the $I_n(x,y)$ maps in parts (a) and (b). (d) Normalized intensities versus bandwidth.

When we include the surface errors of the seven optics and the occulter phase only, we obtain a monochromatic $I_n(x,y)$ map as shown in Fig. 3(a) at λ = 800nm before WFC. After conducting monochromatic WFC for 30 iterations, we obtain a new $I_n(x,y)$ map as shown in Fig. 3(b) with the DM solution shown in Fig. 3(c). The three normalized intensities of this case are shown as a function of control iteration number in Fig. 4(a). If we carry out broadband WFC for the same case, we obtain I_b versus control iteration number curves as shown in Fig. 4(b) at the three wavelengths used. The $I_n(x,y)$ maps at the end of 30 control iterations, the 10%-broadband $I_n(x,y)$ map, and the corresponding DM solution used are shown in Figs. 5(a-c). Also, the broadband normalized intensities are shown as a function of control

bandwidth in Fig. 5(d). As we can see, we can obtain $I_b \approx 1\text{E}-10$ with a bandwidth of 10% in this system. These results are included here as a baseline to the simulations to be presented in the following sub-sections.

In the above WFC simulation, we used an optimized set of four actuator regularization values, $\gamma_{\text{wu}} = [0.1\ 1\ 10\ 100]/\text{nm}^2$, with the corresponding WFC iteration numbers listed in the same order, $N_{\text{WFC}} = [5\ 10\ 10\ 5]$. That is, the WFC process is completed in four phases with four different γ_{wu} values in the order given above, each with a different WFC iteration number also given above.

It should be mentioned that the sensitivity matrix $\widetilde{\mathbf{S}}$ is obtained by including the occulter phase error but setting the surface height errors of the seven optics to zero. Also, the same sensitivity matrix $\widetilde{\mathbf{S}}$ is used in all control iterations, that is, the $\widetilde{\mathbf{S}}$ is not updated or altered during a WFC process, and the same $\widetilde{\mathbf{S}}$ is used in all simulation cases.

3.2 Absorbing Particles on the Flat-Mirror (FM)

The first defect we investigated is the case of absorbing particles on the FM. We assumed 1, 3 and 6 particles having a square shape of width 114μm and heights varying between 10 and 100μm. All particles exhibit the same amount of absorption at a given wavelength, but differing amounts of reflected phase-delays due to different heights. Also, both the reflection coefficient and the phase-delay of those particles change with wavelength. The size of the propagation matrix, 512x512, used in our MACOS simulation tool gives a pixel size of 114μm for the FM, therefore, we chose the smallest possible particle size, varying only the heights, for this category of simulations. The values of the reflection coefficient and the phase-delay of the 6 particles at five different wavelengths are listed in Table 1.

Table 1. Reflection coefficient $r(\lambda)$ and phase-delay $\varphi(\lambda)$ of six absorbing particles on the FM. The optical constants n and k of the particles at 800nm are assumed to be 2.3 and 0.3, respectively.

	Spot #	768nm	784nm	800nm	816nm	832nm
$r(\lambda)$	All	0.4105	0.4065	0.4028	0.3994	0.3963
$\varphi(\lambda)$ [waves]	1	-0.3541	0.3366	-0.0402	-0.4805	0.0193
	2	0.4323	0.0661	-0.3253	0.2596	-0.1779
	3	-0.2695	-0.2744	-0.479	0.1285	-0.4411
	4	0.3652	-0.2036	0.0904	0.2554	0.2987
	5	-0.3825	0.1659	-0.3874	-0.0366	0.2239
	6	-0.0111	0.3869	-0.3509	-0.2165	-0.2025

The MACOS simulation tool does not allow us to place partially-absorbing particles on a reflector. Therefore, we placed the particles on a transparent (transmission-coefficient t = 1 everywhere) virtual surface just before the FM as partially-absorbing spots whose transmission-coefficient is described by $t(x,y;\lambda) = |r(\lambda)|\exp[j\varphi(x,y;\lambda)]$, where the values of $r(\lambda)$ and $\varphi(x,y;\lambda)$ are those listed in Table 1. Figure 6(a) shows the locations of the six particles. The locations are chosen randomly and divided into three groups: One-particle (red), three-particles (red and blue), and six-particles (all colors). We carried out 8%-broadband WFC for these 3 cases, and obtained the 10%-broadband contrast values shown in Fig. 6(b). As a comparison, we included the contrast values of the nominal case where no particle is placed on the FM. The corresponding 10%-broadband $I_n(x,y)$ maps obtained at the end of 30-iterations broadband WFC are shown in Fig. 7(a). To obtain these $I_n(x,y)$ maps, we evaluated the single set of DM solutions at 41 wavelengths, ranging from 760nm to 840nm in an increment of 2nm, so that the interference effects resulting from the finite number of wavelengths are minimized. As we can see from Fig. 6(b), placing just one particle on the FM greatly degrades the broadband contrast, and increasing the number of particles from one to three and six does not make too much difference

on the broadband contrast. As mentioned above, the single set of DM solutions was obtained through a broadband WFC carried out at only three discrete wavelengths. When that set of DM solutions is evaluated at other wavelengths, the particles exhibit completely different phase-delays at the new wavelengths, giving rise to a lot of scattered light inside the dark-hole region.

We also examined a case where no particle is placed on the FM when the initial 30-iterations WFC was carried out, then one particle is placed on the FM, and after that another 30-iterations WFC was conducted. The $I_n(x,y)$ maps at the end of those three steps are shown in Fig. 7(b). In this figure, the left-most $I_n(x,y)$ map has $[C_b\ C_s\ C_m] = [0.49\ 6.9\ 8.3]\times 1E-10$, the middle map $[8.6\ 9.0\ 9.5]\times 1E-9$, and the right-most map $[1.5\ 1.9\ 2.2]\times 1E-9$, respectively. The last contrast values are very close to the 8%-broadband contrasts of $[1.5\ 2.5\ 3.5]\times 1E-9$ of the Particle # = 1 case shown in Fig. 6(b) but obtained by evaluating the DM solutions with five wavelengths.

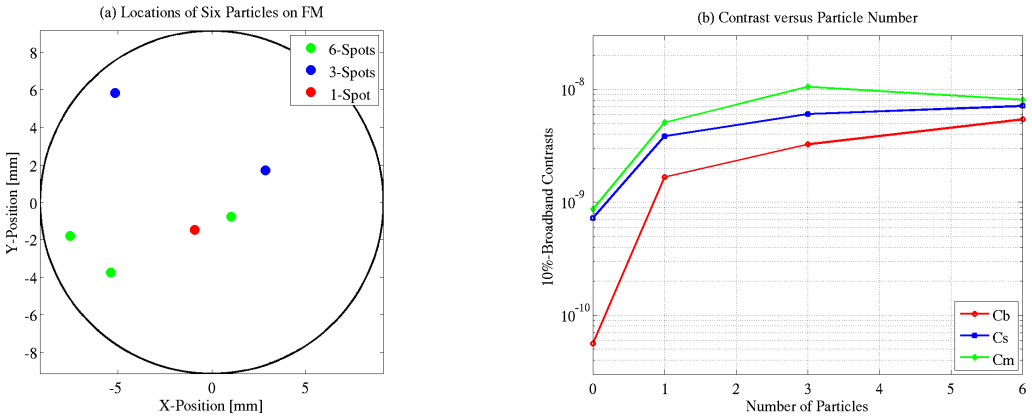

Figure 6. (a) Locations of the six particles on FM. The black-circle indicates the boundary of the FM's illuminated area. (b) 10%-broadband contrasts versus particle number.

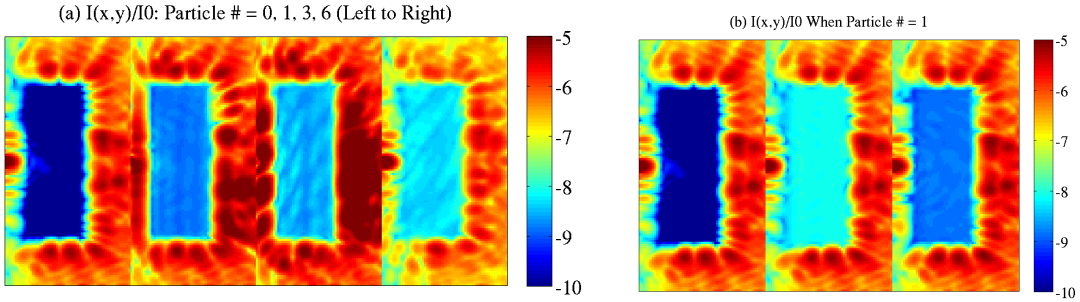

Figure 7. (a) Log-scale 10%-broadband $I_n(x,y)$ maps when the number of the particles placed on FM is 0, 1, 3 and 6, respectively. (b) Log-scale 8%-broadband $I_n(x,y)$ maps when no particle is placed on FM (left), one particle is placed on the FM of the system that achieved the $I_n(x,y)$ map on the left (middle), and after carrying-out another 30-iterations WFC (right).

3.3 Defects on the Occulter Surface

Figure 8(a) shows a portion of the measured image of an occulter fabricated at JPL. A narrow 20μm wide moving slit in close proximity to the substrate surface was employed in a vacuum deposition chamber to coat a thickness profiled layer of Ni on a fused silica substrate. By controlling the dwell time of the slit at a given location, the total thickness of the layer at a given spot to obtain chosen optical density was achieved. Careful thickness calibration runs and multiple passes of the procedure ensured minimum error in fabricating the mask per design as detailed in Refs. [7,12]. However, defects do occur on the occulter as shown in figure 8. In order to understand how the defects on the surface of an actual occulter will affect the broadband contrast of the HCIT, we did the following: (1) Divided the occulter image shown in Fig. 8(a) by its horizontal profile obtained by vertically averaging the same image. (2) Replaced its central, Δx~280μm-wide region with a value of one. We call the resultant map the Occulter Multiplier. (3) Selected two areas from this

Occulter Multiplier, a "good" and a "bad" areas, as indicated by the red- and the yellow-rectangles in Fig. 8(a), and obtained the Occulter Multipliers A and B shown in Figs. 8(b-c), respectively. (4) Multiplied the model Occulter transmittance by those two multipliers, one at a time, and evaluated the resultant 8%-broadband contrast after conducting 30-iterations broadband WFC. That is, we altered the Occulter transmission coefficient by multiplying it with the square-root of the map of Fig. 8(b) or 8(c), but left the Occulter phase unchanged. The resulted $I_n(x,y)$ maps at five different wavelengths (indicated in the figure title) and their average (the right-most part) are shown in Fig. 9. In this figure, the top-row corresponds to the Occulter Multiplier A, and has $[C_b\ C_s\ C_m] = [0.16\ 1.0\ 1.4]\times 1E-9$. The bottom-row corresponds to the Occulter Multiplier B, and has $[C_b\ C_s\ C_m] = [0.50\ 1.2\ 1.6]\times 1E-9$. With these two new occulters, the broadband contrast gets degraded as compared to the nominal case, Figs. 5(a-d), where $[C_b\ C_s\ C_m] = [0.49\ 6.9\ 8.3]\times 1E-10$, and such degradation is more severe with the Occulter B than the Occulter A, as expected. The broadband contrast of HCIT utilizing an occulter similar to Occulter B has been measured by a different group of researchers at JPL, and their measured contrast map has a feature very similar to those of the bottom-row in Fig. 9.

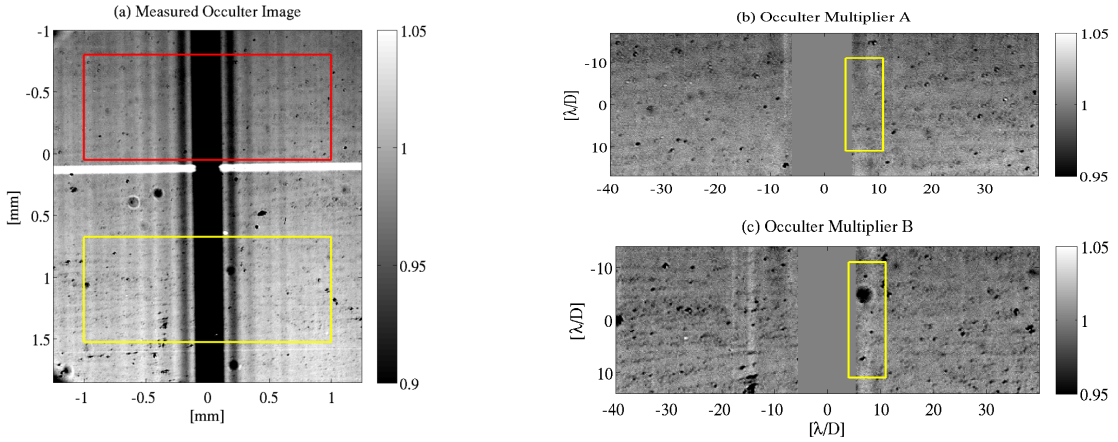

Figure 8. (a) Measured transmittance of an occulter fabricated at JPL. The red- and the yellow-rectangles show a "good" and a "bad" areas on the occulter surface, respectively. (b) An occulter multiplier map obtained from the area of red-rectangle in part (a). The occulter transmission coefficient is multiplied by the square-root of this map to simulate a realistic "good" occulter area. (c) Same as part (b), except that this map is for a "bad" occulter area.

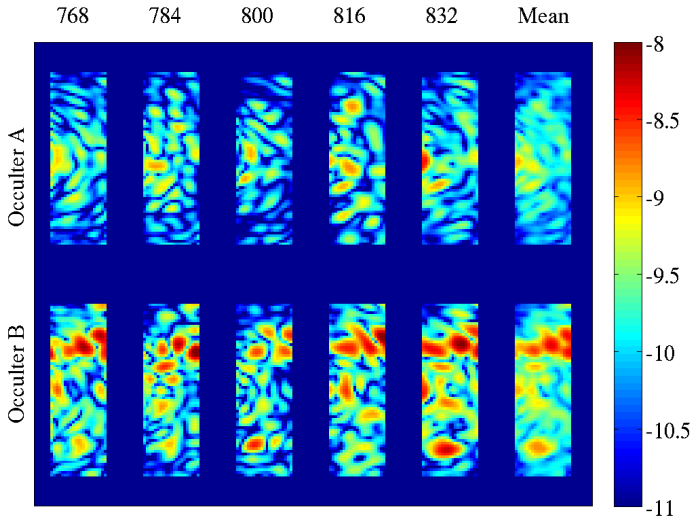

Figure 9. (a) Log-scale $I_n(x,y)$ maps at obtained from the "good" (top) and the "bad" (bottom) occulter areas, respectively. The five left parts of each row correspond to five different wavelengths, and the right-most part is their mean or 8%-broadband $I_n(x,y)$ maps.

3.4 Dead Actuators

Actuator errors affect both the e-field estimation and control. However, there are 2.25 times more actuators in the current HCIT system as compared to those studied in Ref. [6], thus one can expect that the current system is much less sensitive to dead actuators. To confirm this point, we examined the effects of dead actuators on the EFC efficiency only. We chose three cases of dead actuators as shown in Fig. 10(a), where the number of dead actuators, N_{dead}, is equal to 200 (green), 400 (green + blue) and 600 (all colors), respectively. The dead actuators are chosen randomly among the 1907 actuators used. They are not responsive to the applied commands, and remain fixed at the mid-point of their control range. In the current simulations, for the optical system with all seven phase errors, we set the command values of the selected actuators to 0nm (the mid-point of the -200nm to 200nm range) when performing each control iteration. The sensitivity matrix $\tilde{\mathbf{S}}$ is kept the same, but the command values of the dead actuators are set to 0nm.

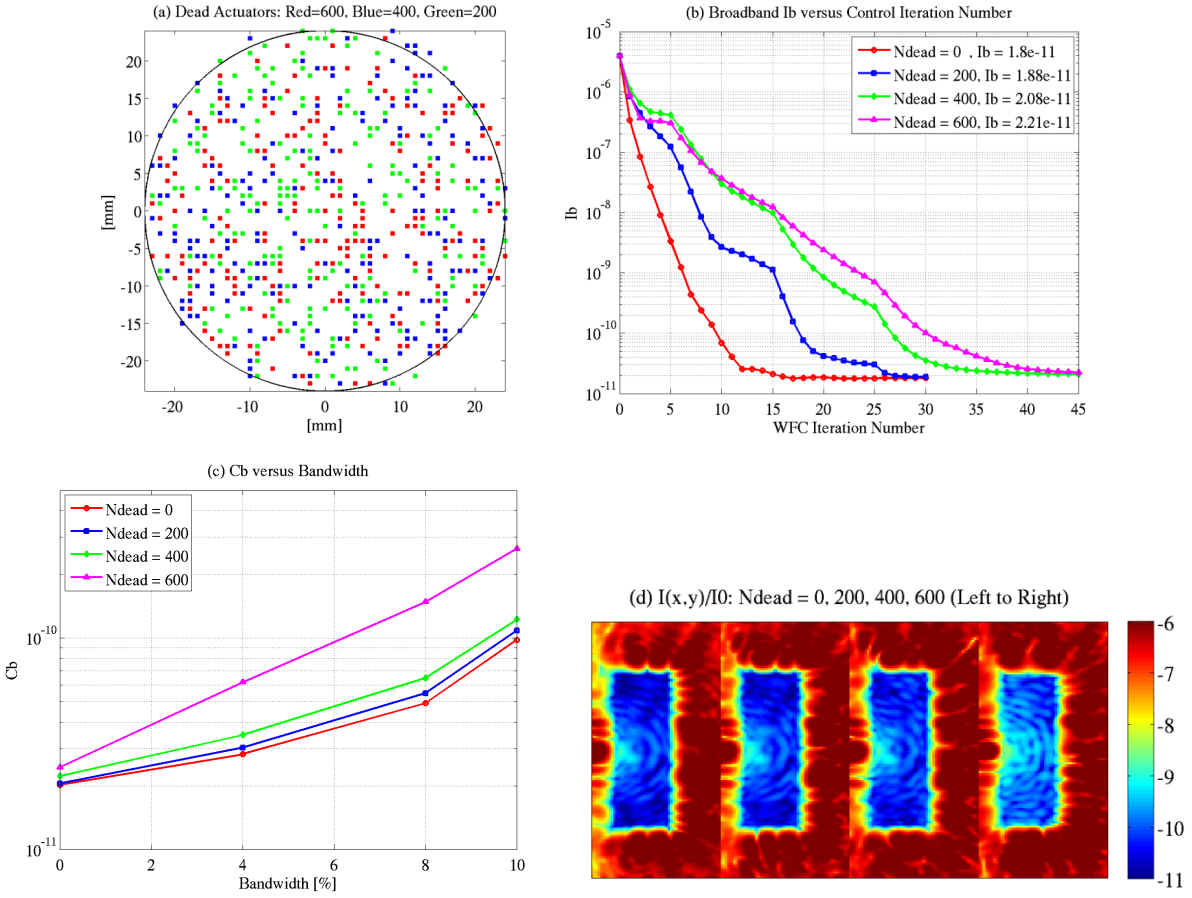

Figure 10. (a) Three groups of dead actuators selected: N_{dead} = 200 (green), 400 (green + blue), and 600 (all colors). (b) I_b versus control iteration number during a 8%-broadband WFC process with N_{dead} as a parameter. Also listed in the figure legend are the I_b values corresponding to the last control iterations. (c) C_b as a function of bandwidth with N_{dead} as a parameter. (d) 10%-broadband $I_n(x,y)$ maps corresponding from the left to the right to N_{dead} = 0, 200, 400, and 600, respectively.

Figure 10(b) compares the WFC efficiency of the following four cases: N_{dead} = 0 (nominal case), 200, 400 and 600. Although what was carried out is 8%-broadband control as in Fig. 4(b), we showed here only I_b as an example. The WFC process becomes less efficient with increasing N_{dead} as expected, but the final value of I_b differs only slightly among the four cases considered. The same is true for C_b versus bandwidth as shown in Fig. 10(c), except the case of N_{dead} = 600 where C_b worsens faster with increased bandwidth than the other three cases. This result is obtained from the 8%-broadband DM solutions corresponding to the last data points in Fig. 10(b). The same DM solutions are used to

obtain the 10%-broadband $I_n(x,y)$ maps shown in Fig.10(d). Again, the first three $I_n(x,y)$ maps are almost identical. That is, as much as 400 dead-actuators do not cause any meaningful reduction in the obtainable 10%-broadband contrast. This is one of the most significant findings of this study. In future work, we will study the effects of actuators that are stuck at one end of their range, as well as actuators that fail in local groups.

3.5 Effects of Control Bandwidth

Carrying-out WFC with a larger bandwidth yields better 10%-broadband contrast, but it takes a longer time to achieve the best level of dark-hole. In order to gain an understanding on the trade-off between the control bandwidth and the best 10%-broadband contrast achievable, we carried out control for the nominal case (all seven phase errors and occulter phase are included) at 0 (monochromatic), 2% and 8% bandwidths, each for 35 iterations, then evaluated the obtained DM solutions at 0, 4, 8 and 10% bandwidths. The 2%-broadband control and the 2%-broadband $I_n(x,y)$ evaluation are done in the same way as the 8%-broadband ones, but with wavelengths of 792, 800 and 808nm, respectively. The results of C_b are shown in Fig. 11(a), and the $I_n(x,y)$ maps at 10%-bandwidth are shown in Fig. 11(b). As we can see from Fig. 11(a), at contrast bandwidth of 10%, C_b of control bandwidth = 0 is about 20 times worse, and that of control bandwidth = 2% is about 2 times worse than the C_b of the control bandwidth = 8%. In the cases of control bandwidth = 2 and 8%, increasing the control bandwidth by a factor of 4 improves C_b by a factor of 2.

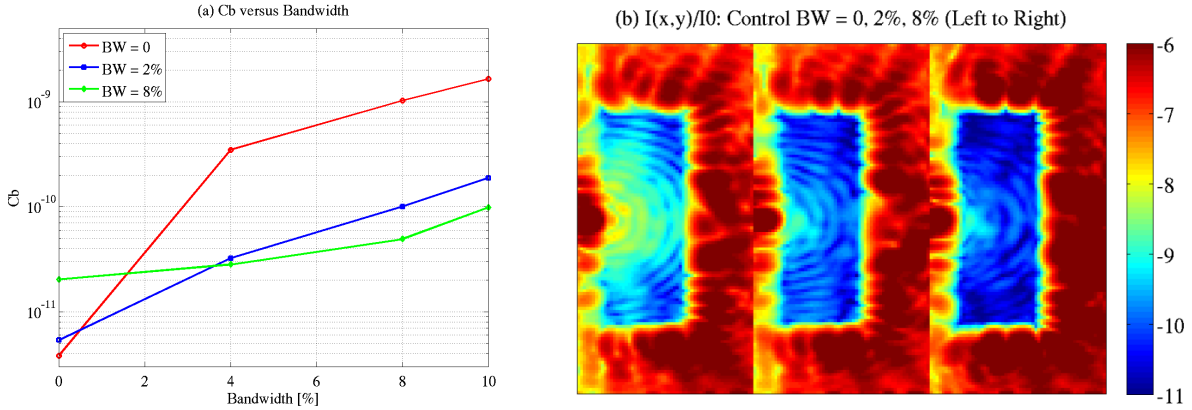

Figure 10. (a) Contrast C_b as a function of contrast bandwidth with control bandwidth (BW in the figure legend) as a parameter. (b) 10%-broadband $I_n(x,y)$ maps corresponding from the left to the right to control bandwidth = 0, 2%, 8%, respectively.

4. CONCLUSION

One of the important milestones of the TPF Coronagraph project is to demonstrate the ability to predict the performance sensitivities of the system at levels consistent with exoplanet detection requirement. In order to gain some general understanding about the potentials and the limitations of the current single-DM HCIT system, we have examined through modeling and simulations the effects of some common errors on the EFC-based control of the e-field over a half dark-hole region. Considered cases include partially-absorbing spots on a flat mirror, defects on the occulting mask surface, and dead actuators of the DM. We have also examined how the control bandwidth affects the 10%-broadband contrast. We have shown that, a single 114μm particle alters both the reflected amplitude and phase of the propagating beam and scatters light into the dark-hole. The resulting speckles can only be nulled partially, and it is impossible to obtain 10%-broadband contrast better than 1E-9 in the presence of one or more such particles. Some defects found on the surface of a fabricated occulter can be very detrimental to the broadband contrast and should be avoided whenever possible. At JPL, a HCIT team has mitigated such a problem by moving the beam center to a "clean" area on the occulter. Current HCIT system utilizing a 48x48 actuators DM is very robust in terms of dead actuators, and up to 400 dead actuators randomly selected did not cause any meaningful degradation to the 10%-broadband contrast. Increasing the control bandwidth does improve the contrast bandwidth. It was found that increasing the control bandwidth from 2% (one 2% bandpass filter) to 8% (three 2% bandpass filters) improves the 10%-broadband contrast by a factor of two at the cost of longer control time.

This work was carried out at the Jet Propulsion Laboratory, California Institute of Technology, under contract with the National Aeronautics and Space Administration.

REFERENCES

1. John T. Trauger, Chris Burrows, Brian Gordon, Joseph J. Green, Andrew E. Lowman, Dwight Moody, Albert F. Niessner, Fang Shi, and Daniel Wilson, "Coronagraph contrast demonstrations with the high-contrast imaging testbed," *Proc. SPIE*, **5487**, 1330 (2004).
2. Andrew E. Lowman, John T. Trauger, Brian Gordon, Joseph J. Green, Dwight Moody, Albert F. Niessner, and Fang Shi, "High-contrast imaging testbed for the Terrestrial Planet Finder coronagraph," *Proc. SPIE*, **5487**, 1246 (2004).
3. Erkin Sidick, Fang Shi, Scott Basinger, Dwight Moody, Andrew E. Lowman, Andreas C. Kuhnert, and John T. Trauger, "Performance of TPF's High-Contrast Imaging Testbed: Modeling and simulations, " *Proc. SPIE*, **6265**, 62653L (2006).
4. Amir Give'on *et al*, "Broadband wavefront correction algorithm for high-contrast imaging system," *Proc. SPIE*, **6691**, 66910A (2007).
5. *Modeling and Analysis for Controlled Optical Systems User's Manual*, Jet Propulsion Laboratory, California Institute of Technology, Pasadena, CA.
6. Erkin Sidick, Stuart Shaklan, Amir Give'on, and Brian Kern, " Studies of the effects of optical system errors on the HCIT contrast performance," *Proc. SPIE*, **8151**, 8151-06 (2011).
7. D. C. Moody and J. T. Trauger, "Hybrid Lyot coronagraph masks and wavefront control for improved spectral bandwidth and throughput," *Proc. SPIE*, 6693, 6693I1-9 (2007).
8. "Exoplanet Exploration Coronagraph Technology: Technology Milestone #2 Report," Brian Kern, Andreas Kuhnert and John Trauger, editors, 8 Aug. 2008, http://exep.jpl.nasa.gov/TPF-C/HCIT-Milestone2Signed-2008-08-08.pdf.
9. K. Balasubramanian, "Band-limited image plane masks for the Terrestrial Planet Finder coronagraph: materials and designs for broadband performance," *Appl. Opt*. 47, pp.116-125 (2008).
10. Erkin Sidick, Scott A. Basinger, and David C. Redding, "An improved wavefront control algorithm for large space telescopes," Proc. SPIE, **7015**, 70154P (2008).
11. E. Sidick, S. Shaklan, A. Give'on, and B. Kern, "Studies of the effects of actuator errors on the HCIT/PIAA contrast performance ," *Proc. SPIE,* **7731**, 7731-4T (2010).
12. D.C. Moody, B.L. Gordon, J.T. Trauger, "Design and demonstration of hybrid Lyot coronagraph masks for improved spectral bandwidth and throughput," *Proc SPIE,* **7010**, 70103P1-9 (2008).